In Fig. 9 we have compared the 84-Mev data for gold obtained at Stanford[5] with calculations for the homogeneous distribution. Here the curves are normalized to the cross section at 35°. For angles less than 110°, good agreement is obtained for a radius given by $r_0=1.10$. The deviation of the three points beyond 110° may be indicative of a fourth moment slightly larger than that for a constant charge density.

In conclusion, the present experimental data for energies below 100 Mev indicate that the mean square radius of the nuclear charge distribution is given by a uniform charge density with $r_0=1.2$. The spread in the experimental data and the uncertainty in the radiative corrections make this determination uncertain by about 10 percent.‡

‡ *Note added in proof.*—Recently the problem of the radiative corrections has received further study by H. Mitter and P. Urban, Acta Phys. Austriaca **8**, 356 (1954); R. Newton, Phys. Rev. **97**, 1162 (1955); H. Suura, Phys. Rev. **98**, 278(A) (1955). Suura's result for the one-photon radiative corrections to high-energy electron scattering is that the leading term (for large momentum transfer and good resolution) of the fractional decrease is given by the Schwinger correction to *all* orders of the Born approximation in the nuclear field.

ACKNOWLEDGMENTS

The author would like to thank Professor A. O. Hanson for helpful comments on the 15.7-Mev data, and Professor R. W. Pidd for permission to quote his new results prior to publication. The assistance of the Joint Computing Group of M.I.T. is gratefully acknowledged, and in particular the skillful work of Mrs. Evelyn Mack. It is a pleasure to thank Professor Herman Feshbach for suggesting and guiding this work. His continued interest and encouragement is greatly appreciated.

PHYSICAL REVIEW VOLUME 98, NUMBER 5 JUNE 1, 1955

Nuclear Cross Sections for 1.4-Bev Neutrons*

T. Coor,† D. A. Hill,‡ W. F. Hornyak,§ L. W. Smith, and G. Snow||
Brookhaven National Laboratory, Upton, New York

(Received January 11, 1955)

Transmission measurements in good and poor geometry have been performed at the Brookhaven Cosmotron to measure the total and absorption cross sections of several nuclei for neutrons in the Bev energy range. The neutrons are produced by bombarding a Be target with 2.2-Bev protons. The neutron detector requires the incident particle to pass an anticoincidence counter and produce in an aluminum radiator a charged particle that will traverse a fourfold scintillation telescope containing 6 in. of lead. Contribution of neutrons below 800 Mev are believed small. The angular distribution of neutrons from the target is sharply peaked forward with a half-width of 6°.

The integral angular distributions of diffraction scattered neutrons from C, Cu, and Pb are measured by varying the detector geometry. The angular half-width of these distributions indicates a mean effective neutron energy of 1.4±0.2 Bev.

The total cross sections σ_H and $\sigma_D-\sigma_H$ are measured by attenuation differences in good geometry of CH_2-C and D_2O-H_2O, with the result: $\sigma_H=42.4\pm1.8$ mb, $\sigma_D-\sigma_H=42.2\pm1.8$ mb.

The cross sections of eight elements from Be to U are measured in good and poor geometry, and the following values of the total and absorption cross sections are deduced (in units of millibarns):

	Be	C	Al	Cu	Sn	Pb	Bi	U
σ_{total}	310	380	700	1390	2200	3210	3280	3640
$\sigma_{\text{absorption}}$	190	200	410	670	1160	1730	1790	1890

Experimental errors are about 3 percent in σ_{total} and 5 percent in $\sigma_{\text{absorption}}$.

An interpretation of these cross sections is given in terms of optical model parameters for two extreme nuclear density distributions: uniform (radius R) and Gaussian $[\rho=\rho_0\exp-(r/a)^2]$. The absorption cross-section data are well fitted with $R=1.28A^{\frac{1}{3}}$ or $a=0.32+0.62A^{\frac{1}{3}}$ in units of 10^{-13} cm. A nuclear density distribution intermediate between uniform and Gaussian will make the present results consistent with the recent electromagnetic radii.

I. INTRODUCTION

THERE has been, in the last few years, a considerable amount of work[1–10] done on the measurement of neutron-nuclei cross sections in the energy range 40–400 Mev. The emphasis has been mainly on transmission measurements in good geometry to measure total cross sections, although in some cases inelastic

* Work performed under contract with the U. S. Atomic Energy Commission.

† Now at Forrestal Research Center, Princeton, New Jersey.

‡ The subject matter of this paper is part of a dissertation presented to the Massachusetts Institute of Technology in partial fulfillment of the degree of Doctor of Philosophy by D. A. Hill. Now at General Electric Laboratory, Schenectady, New York.

§ On leave to the Physics Department, Princeton University, Princeton, New Jersey.

|| On leave to the Physics Department, University of Wisconsin, Madison, Wisconsin.

[1] Cook, McMillan, Peterson, and Sewell, Phys. Rev. **75**, 7 (1949).

[2] Taylor, Pickavance, Cassels, and Randle, Phil. Mag. **42**, 20, 328, 751 (1951).

[3] R. Hildebrand and C. E. Leith, Phys. Rev. **80**, 842 (1950).

[4] R. Hildebrand, University of California Radiation Laboratory Report UCRL-1159, March, 1951 (unpublished).

[5] Bratenahl, Fernbach, Hildebrand, Leith, and Meyer, Phys. Rev. **77**, 597 (1950).

[6] J. DeJuren and N. Knable, Phys. Rev. **77**, 606 (1950).

[7] J. DeJuren, Phys. Rev. **80**, 27 (1950).

[8] Fox, Leith, Wouters, and MacKenzie, Phys. Rev. **80**, 23 (1950).

[9] W. P. Ball, University of California Radiation Laboratory Report UCRL-1938, August 1952 (unpublished).

[10] V. A. Nedzel, Phys. Rev. **94**, 174 (1954).

and differential cross sections have also been measured. Much of the previous data has been summarized by Rossi,[11] Hildebrand,[12] and recently by Nedzel.[10] It has been shown[1] that neutron-nuclei cross sections exhibit a considerable transparency in this energy range. It is possible with the aid of suitable models of the nucleus to extract information from these data bearing on the size and gross structure of the nucleus. In addition, the neutron-proton and neutron-deuteron cross sections are of particular interest since any theory of nuclear forces must be able to explain these elementary interactions and their dependence on energy.

The interpretation of neutron-nuclei cross sections has to date been confined to extremely simplified models. For example, at the lower energies the analysis of Feshbach, Porter, and Weisskopf[13] pictures the nucleus as characterized by an average complex (absorptive +scattering) potential. A partial wave analysis using this potential has had considerable success in explaining the trend of the total and absorption cross sections at lower energies. At higher energies, however, a partial wave analysis becomes unwieldy. Fernbach, Serber, and Taylor[14] introduced the "optical model" by making the classical approximation that at high energies the wave normals (particle trajectories) are only slightly deflected in passing through nuclear matter. In this model the nucleus is described as having some radial density distribution, an absorption constant K, and a refractive index $(k+k_1)/k$ (where k_1 is the increment in the propagation constant within nuclear matter). This model has been shown to be equivalent to a partial wave analysis using the WKB approximation and is expected to become more valid as the energy increases.

Charged particles such as protons may also be used as a probe for exploring the nucleus, however, with the disadvantage that the observed effects are due to a combination of Coulomb and nuclear interactions.[15,16] (The scattering experiments using electrons, of Hofstadter *et al.*,[17] involve only Coulomb effects and give information as to the *charge* distribution within the nucleus.) The use of neutrons, on the other hand, increase the experimental difficulties because of the low efficiency and poor energy resolution of practical neutron detectors.

The present experiments were performed with neutrons having an average energy, weighted by the detector efficiency, of 1.4 Bev. At this energy essentially all of the diffraction scattering is contained within a cone of less than 6° half-angle even for the light nuclei. Hence it becomes relatively easy to measure in addition to the total cross section, the absorption cross section in "poor" geometry. It is also possible to measure the cross sections at intermediate points, which determine the integral angular distribution of diffraction scattering. Interpreted in the light of the optical model, using an assumed nuclear density distribution and the measured free nucleon-nucleon cross section, such experimental data yield values of the mean neutron energy, the nuclear radius, and the change of the incident neutron propagation constant within nuclear matter.

II. EXPERIMENTAL APPARATUS AND ANALYSIS OF THE BEAM

(a) Neutron Source

The Brookhaven Cosmotron[18] provides an internal beam of approximately 10^{10} protons per pulse with 2.2-Bev energy. By slowly turning off the radio-frequency voltage at the end of the acceleration cycle, the protons are made to hit an internal target over an interval of 30 milliseconds. The acceleration cycle is repeated every 5 seconds. In this experiment, a 6-in. beryllium target was used in order to maximize the number of high-energy neutrons coming from the target. The neutrons that emerge at 1° to the direction of the incident proton beam, the most forward unobstructed angle, are collimated by a 1 or 2 inch diameter hole extending through 8 feet of shielding concrete and 2 feet of lead. A plan view of the Cosmotron is shown in Fig. 1.

(b) Neutron Detector

Neutrons were detected by requiring that they traverse an anticoincidence counter A and produce in a 2 in. aluminum radiator, charged particles which penetrate a fourfold scintillation counter telescope containing 6 in. of lead. The fourth counter subtends an angle of $\pm 4.3°$ at the center of the radiator. The telescope is illustrated in Fig. 2.

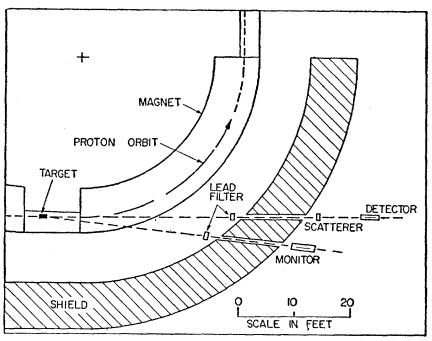

FIG. 1. Plan view of the NE quadrant of the Cosmotron, showing experimental arrangement.

[11] B. Rossi, *High-Energy Particles* (Prentice-Hall Inc., New York, 1952).
[12] Hildebrand, Hicks, and Harker, University of California Radiation Report UCRL-1305, 1951 (unpublished).
[13] Feshbach, Porter, and Weisskopf, Phys. Rev. **96**, 448 (1954).
[14] Fernbach, Serber, and Taylor, Phys. Rev. **75**, 1352 (1949).
[15] F. Chen, thesis, Harvard University, 1954 (unpublished); Chen, Leavitt, and Shapiro (to be published).
[16] J. M. Cassels and J. D. Lawson, Proc. Phys. Soc. (London) **A67**, 125 (1954).
[17] Hofstadter, Fechter, and McIntyre, Phys. Rev. **92**, 978 (1953).
[18] Cosmotron Staff, Rev. Sci. Instr. **24**, 723 (1953).

Both energetic protons and mesons are produced in the aluminum. A proton needs an energy of 400 Mev to traverse this telescope. Hence, 400 Mev is the absolute energy threshold for neutron detection, corresponding to an elastic charge exchange scattering of a neutron and a proton in the aluminum radiator. A charged meson needs 240 Mev to traverse 6 in. of lead, but this requires an incident neutron of at least 540 Mev.

Several preliminary measurements were made on the response of the telescope to different radiators and different thicknesses of lead absorber. Aluminum was chosen since it gave the largest counting rate per unit length of material. The thickness of lead absorber was chosen as a compromise between a high-energy threshold and a high detection efficiency. For lead absorbers thicker than a few inches the counting rate decreases exponentially with an absorption length corresponding approximately to the geometric absorption cross section. This fact suggests that only a small fraction of the neutron detected have energies less than ~800 Mev. A substantial increase in the threshold energy would have resulted in a prohibitive loss in counting rate, e.g., a 1-Bev proton has a range in lead of more than three absorption lengths. Some bias in favor of the detection of higher energy neutrons is obtained from the smallness of the angle subtended by the last counter with respect to the aluminum radiator.

The plastic scintillators are compression molded from polystyrene activated with terphenyl and a trace of diphenylhexatriene. The electronic circuitry is of standard design. The photomultiplier tubes are selected 1P21's which operate without breakdown at anode potentials up to 2000 volts. Each output signal is limited to about 2 volts with a biased crystal diode to prevent overloading, and is led through 100 feet of cable to a wide band, distributed amplifier (Hewlett-Packard Model 460 B). The fourfold coincidence signal with anticoincidence from A is formed in circuit of the type described by Garwin,[19] is amplified, and then enters a fast discriminator circuit using an EFP 60 secondary emission tube. The output pulses drive a fast scale of eight followed by a one microsecond scale of sixty-four and register. The integral bias curve obtained with this circuit shows a very satisfactory plateau for fourfold coincidences and an anticoincidence counter

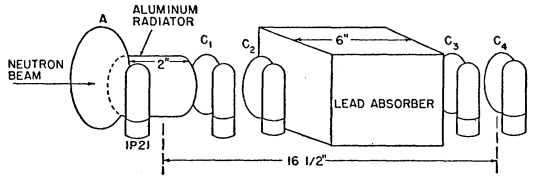

FIG. 2. Neutron detector. Coincident counters C_1-C_4 are plastic scintillators $2\frac{1}{2}$-in. in diameter and $\frac{1}{2}$-in. thick. Anticoincidence counter A is plastic scintillator 4 in. in diameter and $\frac{1}{2}$ in. thick.

[19] R. Garwin, Rev. Sci. Instr. 24, 618 (1953).

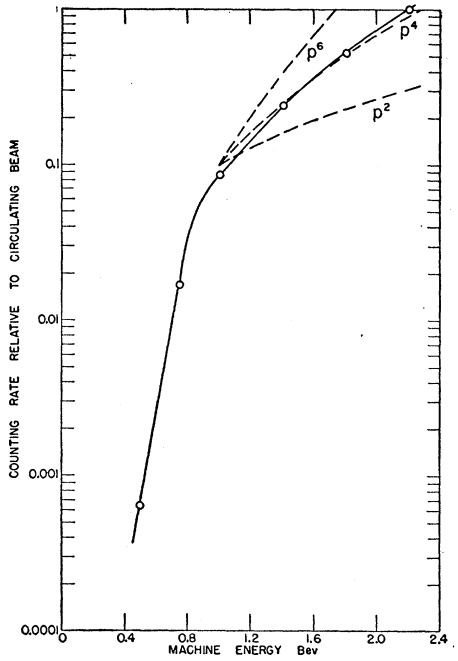

FIG. 3. Energy excitation function of the standard neutron detector. The ratio of the neutron detector counting rate to the proton circulating beam current is shown *vs* the incident proton energy. The neutrons emerge from a 6-in. Be target at 1° to the incident proton direction. Above 1 Bev the excitation function is proportional to p^4, where p is the incident proton momentum.

efficiency of greater than 0.99. The circuit is gated on only during the time that the beam strikes the target.

The measured resolving time of the coincidence circuit is about 8×10^{-9} second (half-width at half-maximum response) and is determined by the decay time of the scintillator; improvement by pulse clipping has not been necessary. The amplifier and discriminator following the coincidence circuit have a measured recovery time of 8×10^{-8} second; the counting speed is limited by the scale of eight which has a recovery time of 2×10^{-7} second. With typical beam intensities, we obtain 10 to 20 counts in a 30-millisecond interval. The expected counting losses based on this average rate are negligible; however, the peak counting rates in this interval may be many times larger due to "bunching" of the internal proton beam. Bunching is observed corresponding to the 1-kc synchroton oscillations; whether this also occurs with the higher frequency of betatron oscillations is not known at present.

A monitor of the beam intensity is provided by a threefold counter telescope placed outside the shield in a beam which emerges at 3° to the forward direction. The telescope contains $1\frac{1}{2}$ inches of lead and is placed behind a 10-inch Lucite radiator. The counting rate is roughly 200 per pulse and is attributed mainly to neutron conversion in the Lucite since the counting rate with the Lucite removed is several times smaller. The construction and circuitry for the monitor is similar

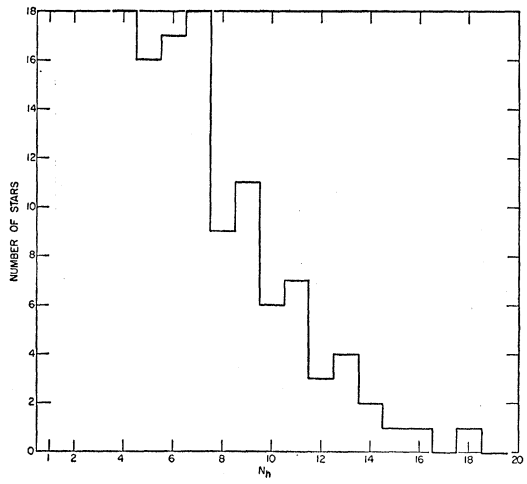

FIG. 4. Prong number distribution of neutron stars produced by forward neutrons from Be bombarded by 2.2-Bev protons. N_h is the number of gray plus black prongs (some minimum prongs included).

to that of the detector except that it does not have an anticoincidence counter.

To get some idea about the dependence of the neutron detection efficiency on energy, the ratio of the detector counting rate to the circulating proton beam current was measured as a function of machine energy, as shown in Fig. 3. (The proton beam current was monitored by measuring the voltage induced on a pair of pickup electrodes through which the beam passed.) This steeply rising function of energy represents the product of two probabilities: first, the probability that a proton striking the beryllium target will produce an energetic neutron in the forward direction and second, the probability that this neutron will produce in the aluminum radiator an energetic charged secondary in the forward direction. If recoil protons, both inelastic and elastic, cause most of the counts in the neutron telescope the first and second probabilities are quite similar. Hence, the p^4 dependence from 1 to 2 Bev, as shown in Fig. 3, suggests a neutron detection efficiency proportional to p^2. The fact that the counting rate falls off much more rapidly below 0.9 Bev suggests that the effective threshold of this neutron detector is substantially higher than the absolute threshold of 0.4 Bev. One simple explanation of the p^2 energy dependence is that the half-angle of the forward cone of recoil protons, both elastic and inelastic, decreases with energy proportional to $1/p$, so that the fractional probability for a proton to traverse a fixed solid angle in the forward direction increases approximately as p^2.

(c) Neutron Flux and Angular Distribution

A crude estimate of the neutron flux was obtained by exposing Ilford G5 emulsions in the collimated neutron beam at the position of the detector. Area scanning led to the star prong number distribution shown in Fig. 4. The mean free path for the production of events with $N_h \geq 9$ by 2.2-Bev protons has been measured[20] to be 190 cm of Ilford G5 emulsion. For neutrons, we adopt this mean free path for star production with $N_h \geq 8$, and hence obtain a flux of neutrons that can make 8-prong stars of about 10^3 neutrons per cm^2 per pulse. The average energy released among the slow secondaries in an 8-prong event is ~550 Mev. This energy is not very different from the energy threshold of the telescope. A comparison of this deduced flux with the observed counting rate in the telescope detector implies a detection efficiency of about 0.1 percent.

The angular distribution of energetic neutrons produced in the beryllium target was measured by moving the detector around to various ports in the shielding which view the target. Figure 5 shows the results obtained at two accelerated proton energies after correcting the observed counting rates for the varying thickness of obstruction in the neutron path (up to 28 percent correction) and the slightly different distances from the target to the detector (up to 9 percent correction). The distribution is strongly peaked in the forward direction. At 2.2 Bev, the half-width at half-maximum is 6.5°. The distribution is similar to that observed at Berkeley[21] with 340-Mev protons on a beryllium target if the angle scale is reduced with a factor of 3.5. This factor is just equal to the ratio of

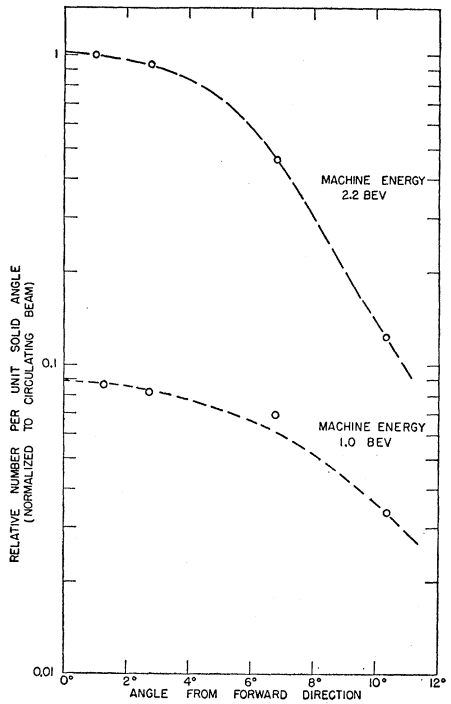

FIG. 5. Angular distribution of energetic neutrons from Be bombarded by protons of 2.2 Bev and 1.0 Bev. The energy excitation function of the neutron detector is shown in Fig. 3.

[20] M. Widgoff (private communication).

[21] J. DeJuren, University of California Radiation Laboratory Report UCRL-773 (unpublished).

the incident proton momenta (lab system), and hence agrees with the previous explanation of the energy excitation function of the detector.

(d) Production of Penetrating Charged Secondaries by Neutrons

For comparison, the angular distribution of penetrating charged secondaries produced in beryllium, aluminum, and lead was measured with the arrangement shown in Fig. 6. The difference in counting rate with the sample in and out was measured for several angles up to 20°. Figure 7 presents the observed angular distributions from beryllium, aluminum, and lead. The angular resolution, as determined by the half-angle subtended by the last counter C_4 at the converter, is 4.2°. The angular distribution is again peaked forward and sensibly the same for these three elements. The relative yield per nucleus varies approximately as $A^{\frac{1}{3}}$, which suggests that mainly the nucleons around the perimeter of the nucleus contribute to the process giving rise to the penetrating charged particles. The measurements described above would be in error if an

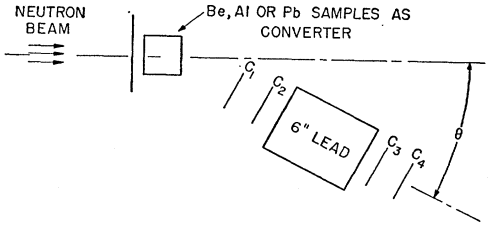

FIG. 6. Telescope arrangement for the measurement of the angular distribution of energetic charged secondaries produced by incident neutrons in beryllium, aluminum, and lead.

appreciable number of incoming neutrons interact not in the sample but in the 6-in. lead absorber giving rise to charged particles going forward to trip counters 3 and 4 and charged particles going backward to trip counters 1 and 2. This effect was estimated by putting the fourfold telescope in the beam and moving counters 1 and 2 out of the beam so that a single particle going forward from the converter cannot traverse 1, 2, 3, and 4, but a single backward-going particle from the lead can traverse 1 and 2. The contributions from events of this type constitute at most 6 percent of the observed counting rate.

(e) Collimation of the Neutron Beam

The forward neutron beam was collimated by either a 1-in. or 2-in. hole extending through 8 ft of shielding concrete and 2 ft of lead. The effectiveness of collimation for the 1-in. hole can be seen in Fig. 8 which shows the detector counting rate *versus* lateral displacement at a distance of 12 ft from the collimator. The measured dependence agrees with that expected from the overlap of a 1 in. diameter beam with a $2\frac{1}{2}$-in. diameter detector. With the detector aligned in the beam, the counting

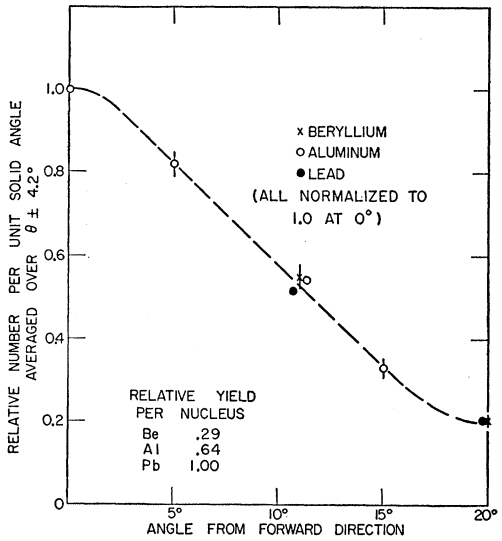

FIG. 7. Angular distribution of energetic charged secondaries produced by neutrons in beryllium, aluminum, and lead. The angular resolution is ±4.2°. The relative yield per nucleus varies approximately as $A^{\frac{1}{3}}$.

rate decreases by (3.5±2 percent) as the detector is moved from 3 feet to 12 feet from the collimator.

III. EXPERIMENTAL PROCEDURE AND RESULTS

(a) Hydrogen and Deuterium Total Cross Sections

Using the 2-in. diameter collimated neutron beam described in the last section, the total *n-p* cross section was determined by measuring the difference in the attenuation in good geometry of polyethylene $(CH_2)_n$, and carbon. The samples used were of high purity and were chosen to contain the same number of grams per cm² of carbon. The difference $\sigma_D - \sigma_H$ was measured in the same way with samples of heavy water (D_2O) and

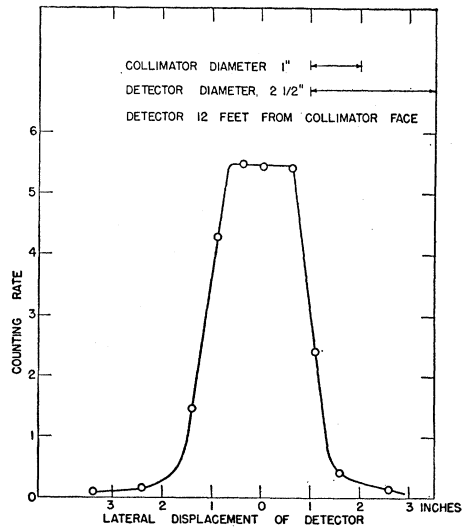

FIG. 8. Neutron beam profile for the 1-in. diameter collimator.

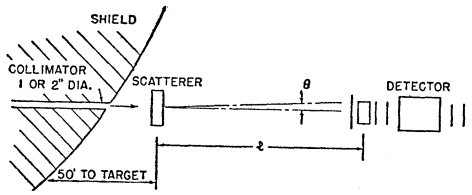

FIG. 9. experimental arrangement for transmission measurements. θ is the angle subtended at the scatterer by the Al radiator in the neutron detector.

ordinary water contained in thin walled brass cylinders of equal length. Figure 9 shows the disposition of scatterer and detector. The half-angle θ subtended by the detector at the scatterer was normally about 0.7°; the divergence of the incident beam is of the order of 0.2°. Data was collected by alternating the samples after about 5000 counts were recorded in the detector. The beam monitor was run concurrently and, in all cases, only the ratio of detector to monitor counts was used. One day's run comprised about 100 000 counts taken in this way.

The experimental arrangement was varied in the second *n-p* run by doubling the thickness of carbon and polyethylene used. In the third *n-p* run, the collimated beam was reduced to 1-in. diameter. The geometry was varied slightly in the second D_2O-H_2O run by increasing the angle subtended by the detector to 1.6°. Table I summarizes the results of five runs and gives the weighted average value with the estimated error. The mean effective neutron energy for this experiment is taken to be 1.4±0.2 Bev. This result is calculated from the half-width of the observed angular distribution of diffraction-scattered neutrons from C, Cu, and Pb and is discussed in more detail in the next section.

(b) Cross Sections of Heavier Elements

Measurements of the absorption cross sections and the total cross sections of eight elements, Be, C, Al, Cu, Sn, Pb, Bi, and U, were made. The integral angular distributions of the elastically scattered neutrons from C, Cu, and Pb were also determined. The thickness of each sample was chosen to be about one half an absorption length. This choice is a compromise between minimizing the multiple scattering effects and maximizing the statistical accuracy of the cross-section measurement.

TABLE I. Summary of CH_2-C and D_2O-H_2O results.

Run	Thickness of carbon (H_2O) in mean free paths	θ	Measured σ (mb)	Background correction (mb)	Observed standard deviation (mb)	Expected standard deviation (statistics only) (mb)
I CH_2-C difference						
7–24	0.56	0.66°	45.6	+0.2	±3.6	±3.3
7–30	1.02	0.68°	41.0	0.2	1.8	1.8
2–5	0.56	0.66°	47.3	0.5	6.3	3.5
II D_2O-H_2O difference						
7–25	1.09	0.67°	44.7	+0.2	±2.2	±2.2
7–29	1.09	1.5°	39.7	0.2	2.0	2.0

III Weighted averages including estimate of systematic error
Total cross sections for 1.4±0.2 Bev neutrons:
$\sigma_H = 42.4 \pm 1.8$ mb, $\sigma_D - \sigma_H = 42.2 \pm 1.8$ mb.

The experimental arrangement is shown in Fig. 9. The neutron beam was collimated to a 1-in. diameter. The detector was displaced horizontally and vertically until the maximum counting rate was obtained and then held fixed. Data was collected by changing the scatterer or the geometry after about 2500 counts were recorded. Following every three or four such runs, 2500 counts were taken with the scatterer removed. For the three elements, C, Cu, and Pb, transmission measurements were made with the scatterer placed at distances ranging from 6 in. to 30 ft from the detector. In this way the half-angle, θ, subtended by the detector at the scatterer was varied from 12° to 0.2°. The values of these measured transmissions, as a function of θ are shown in Figs. 10, 11, and 12. The transmission measured in "good" geometry ($\theta = 0.2°$ to 0.5°) determines the total nuclear cross section, σ_T. As θ increases, more and more of the very small-angle, elastically diffracted neutrons impinge on the detector and hence do not contribute in first approximation to the attenuation of the neutron beam. For $\theta \geq 6°$ the measured transmission remains constant, which indicates that what is being measured is just the absorption cross section, σ_a. This possibility of measuring the nuclear absorption cross section directly is one of the unique advantages of measuring nuclear cross sections with very high-energy neutrons. To obtain more accurate values for σ_a, the measured transmission must be corrected for the dependence of the telescope efficiency on incident neutron angle. This correction is shown on Figs. 10–12 and is discussed in detail in Sec. III(c). The shape of the transmission curves in the intermediate angular region can

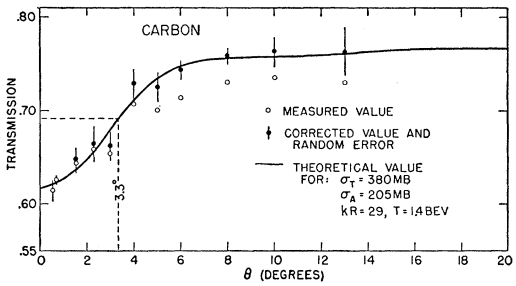

FIG. 10. Neutron transmission for carbon as a function of the angle, θ, subtended by the detector at the scatterer. Carbon sample thickness = 25.47 g/cm². The measured transmissions and the values of the transmissions corrected for the variation of neutron detection efficiency with incident neutron angle are shown. (A detailed discussion of these corrections are given in Appendices A and B.) The solid curve corresponds to a uniform-sphere diffraction scattering cross section for neutrons of 1.4 Bev, as described in Sec. IV.

be used to determine the average energy of the incident neutrons, as shown in Sec. IV.

The same experimental arrangement was used to measure the attenuation of the other five elements Be, Al, Sn, Bi, and U. These were done in good geometry (0.21°–0.55°) and bad geometry (6°–10°) only. The experimental results at typical good- and bad-geometry angles, $\theta=0.55°$ and $\theta=6°$, respectively, are listed in Table II.

(c) Corrections and Errors

There are two instrumental effects which introduce an important systematic error in the poor-geometry measurements and for which a correction to the data has been made:

Directionality of the Detector

The arrangement of the detector is such that the efficiency of detection is dependent on the angle which the incident neutron makes with the axis of the detector. In general, the scattered neutrons which enter the detector in a diverging cone are counted with reduced efficiency relative to the unattenuated neutrons which enter parallel to the axis. The dependence of the detection efficiency on angle was measured directly by observing the counting rate as the detector is inclined at various angles to the collimated beam, the radiator remaining fixed in the beam. The result is the angular distribution of penetrating secondaries produced in aluminum (shown in Fig. 8). This shows, for example, that the detection efficiency falls off to half-maximum for neutrons entering the detector at an angle of 11° to the axis. The correction to the observed transmission at a given half-angle, is computed by averaging the measured relative efficiency with an approximate diffraction scattering angular distribution over the angular interval $0°-\theta$. Then that portion of the observed transmission which is due to scattered particles, i.e., $[T(\theta)-T(0)]$, is increased, so as to compensate for this calculated reduced efficiency. The correction is largest for the light elements: it amounts to 13 percent of σ_a in carbon, 3 percent of σ_a in lead.

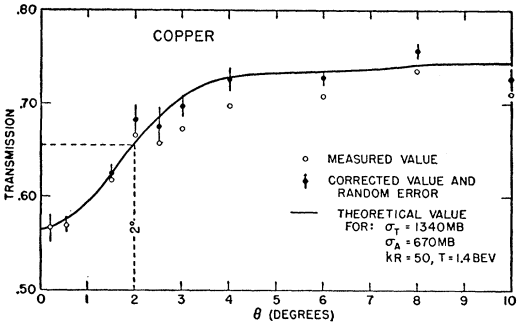

FIG. 11. Neutron transmission *vs* θ for copper (43.40 g/cm²). See caption of Fig. 10.

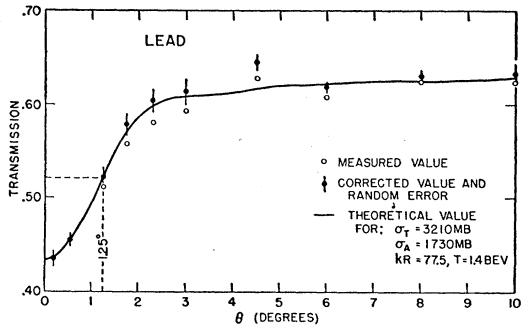

FIG. 12. Neutron transmission *vs* θ for lead (89.78 g/cm²). See caption of Fig. 10.

In good geometry the correction becomes negligible and hence does not affect σ_T. Appendix A discusses the calculation in more detail.

Finite Beam Size

In this experiment, the diameter of the collimated beam (1 in.) is not negligibly small compared to the aperture of the detector ($2\frac{1}{2}$ in.). Therefore, account must be taken of the fact that the probability g, that a particle scattered through an angle ξ shall enter the detector, depends upon ξ, upon the half-angle of collection θ, and upon the distance ρ from the axis at which the scattering occurs. Under the simplifying assumption that the detector efficiency is independent of angle and uniform over the $2\frac{1}{2}$-in. aperture, the detector probability, g, is suitably averaged over an approximate angular distribution and over the cross section of the incident beam. Then a compensating correction is made to relate the observed transmission to the idealized case of a collimated beam of zero width. The correction to the transmission amounts at most to 6 percent of the contribution to the measured transmission from diffraction scattered particles, i.e., $T(\theta)-T(0)$. This maximum correction occurs in the region where T *vs* θ is rapidly rising. The correction is the same for all elements at corresponding points of the diffraction pattern and vanishes in both good and bad geometry limits in all cases. Details of the calculation are given in Appendix B.

TABLE II. Observed and corrected transmissions (T and T', respectively) at $\theta=0.53°$ and 6°, and the corresponding corrected cross sections.[a]

Element	Sample thickness (g/cm²)	$\theta=0.55°$ T	T'	σ(mb)	$\theta=6°$ T	T'	σ(mb)
Be	18.80	0.681	0.681	306	0.755	0.776	202
C	25.47	0.614	0.614	382	0.712	0.743	234
Al	41.20	0.532	0.533	685	0.643	0.666	446
Cu	43.40	0.569	0.570	1370	0.708	0.728	770
Sn	62.62	0.512	0.512	2110	0.660	0.673	1240
Pb	89.78	0.453	0.455	3020	0.608	0.618	1850
Bi	87.18	0.459	0.460	3090	0.614	0.622	1890
U	72.57	0.529	0.531	3430	0.681	0.691	2010

[a] Error in T' varies from 1.2 to 2.1 percent. Error in $\sigma(6°)$ varies from 2.6 to 6.4 percent. Error in $\sigma(0.55°)$ varies from 1.7 to 4.2 percent.

Several other possible sources of errors have been considered of which the most important are the following:

Random Errors

In the CH_2-C and D_2O-H_2O difference experiments, each day's run consists of about 10 groups of 5000 counts for each sample. The observed rms deviation from the mean of the ten groups ranges from 1.0 to 1.8 times the deviation expected from statistical fluctuations only. The excess fluctuation may arise from instability of the electronic equipment or it may reflect the variable operating conditions of the Cosmotron.

For the transmission measurements on the elements Be, C, $\cdots$U, all the data obtained over a six-month period were analyzed for fluctuations from the mean value. The observed rms deviations are, on the average, about 1.6 times the expected deviation due to statistics only.

Rate Effects

Chance coincidences and dead-time effects in the coincidence or scaling circuits can cause a systematic error in the transmission. An experimental estimate of the chance coincidence rate was made by delaying the signal from one counter by 2.5×10^{-8} second or about three times the resolving time. This accidental rate was 0.8 percent of the normal counting rate. This would suggest an error in the measured transmission of less than 0.3 percent. Counting losses due to dead time in the anticoincidence counter or the discriminator and scaling circuits are estimated to be negligible. In the normal course of operation, data were taken with beam intensities that varied by factors as large as 10. Analysis of the measured values of transmission shows fluctuations in excess of statistics but these fluctuations do not appear to be correlated with beam intensity. Effects of the order of 1 percent or less cannot be excluded.

Charged Particles

The presence of charged particles in the neutron beam caused the observed counting rate to increase 50 percent when the anticoincidence counter was disconnected. (The ratio of charged particles to neutrons in the beam was of the order of 0.1 percent. Their contribution to this counting rate is large because of the poor efficiency for detecting neutrons, $\sim$0.1 percent.) The measured efficiency of the anticoincidence counter is 0.99 or greater. Therefore, the maximum effect due to charged particles is about 0.5 percent of the measured transmission. The maximum effect is realized in the good-geometry measurements on the heavy elements; in this case the charged particles are almost completely removed from the detected beam because of Coulomb scattering. In the poor geometry measurements, the effect is probably negligible since the absorption cross section for the charged particles if they are protons or pions, is presumably not much different than that for neutrons.

Background

When the neutron beam was attenuated with a column of lead 3 in. wide and 52 in. thick a residual background counting rate of about 0.4 percent of the unattenuated beam was observed. The effect of this is to make the observed transmissions systematically too large by about 0.2 percent.

Gamma Rays

The number of gamma rays detected in the neutron telescope is believed to be negligible. On the average, it would require a gamma ray of 50 Bev to produce a shower capable of penetrating 6 in. of lead (27 radiation lengths). Furthermore, a $1\frac{1}{2}$-in. lead filter (6.7 radiation lengths) was placed in the beam between the target and the collimator (see Fig. 1). It was shown with the use of a gamma-ray detector that this lead filter substantially removed the gamma rays from the beam.

Secondaries

A priori, one might expect that secondary neutrons from the sample scatterer would make an appreciable contribution to the counting rate in poor geometry. Furthermore, this contribution is intrinsically difficult to measure directly. There are two indirect pieces of data that strongly suggest that the secondary neutrons make a very small contribution to the counting rate. The first is that a plateau is observed for the transmission of Pb, Cu and, less strikingly, for C, in poor geometries ($\theta=6°$ to 10°). If the neutral secondaries made a significant contribution one would expect a rise in the transmission as θ increased. The second point is that the measured number of *charged* secondaries energetic enough to penetrate 6 in. of Pb is very small. Using the very rough calibration of the incident neutron flux described in Sec. II(c), and the measured number of charged secondaries from Be, Al, and Pb, described in Sec. II(d), one can deduce a cross section, $\sigma_S(8°)$, for the production, within an angle of 8°, of charged secondaries capable of penetrating 6 in. Pb. The values of $\sigma_S(8°)$ are 6.5, 14, and 22 mb for Be, Al, and Pb, respectively. These cross sections have a relative accuracy of about ±5 percent, and an absolute accuracy of about a factor of two. These cross sections are only 3.4, 3.4, and 1.2 percent of the measured absorption cross sections of Be, Al, and Pb, respectively. Hence if one assumes that the number of energetic secondary neutrons are comparable to the number of energetic secondary charged particles, their contribution to the measured cross section in poor geometry is small. This assumption is certainly a conservative one for interactions in which one or two mesons are made. In such cases, the number of secondary neutrons will be considerably smaller than the number of secondary charged particles (protons

TABLE III. Summary of measured nuclear cross sections and the derived optical model parameters for a uniform nuclear density.[a]

	Measured quantities				Derived for $\bar{\sigma}=43$		Derived for $\bar{\sigma}=30$	
	σ_a	σ_T	σ_d	σ_T/σ_a	K	R	K	R
Be	187±12	308±13	121± 18	1.65±0.13	0.41	2.83±0.21	0.15	3.50
C	201±13	378±10	177± 16	1.88±0.12	0.58	2.76±0.14	0.26	3.20
Al	414±23	703±18	289± 29	1.70±0.10	0.47	3.89±0.15	0.25	4.26
Cu	674±34	1388±39	714± 52	2.06±0.12	0.60	4.77±0.14	0.38	4.95
Sn	1158±63	2202±62	1044± 88	1.90±0.12	0.50	6.23±0.18	0.32	6.40
Pb	1727±45	3209±55	1482± 71	1.86±0.06	0.49	7.55±0.11	0.33	7.68
Bi	1793±55	3275±62	1482± 83	1.83±0.07	0.47	7.71±0.13	0.31	7.85
U	1887±98	3640±91	1753±134	1.93±0.11	0.50	7.89±0.22	0.33	8.01

[a] All cross sections are in units of 10^{-27} cm^2. R is in units of 10^{-13} cm. K is in units of 10^{13} cm^{-1}.

plus mesons). A further reduction of the secondary neutron contribution relative to the measured number of charged secondaries will be made by the anticoincidence counter in the neutron telescope, since any secondary neutron accompanied by a charged particle will not be counted. It should be noted here that the number of energetic charged secondaries does not form an upper bound to those neutrons that are scattered inelastically but coherently, e.g., neutrons that leave the target nucleus in a low-energy excited state. However, such coherent inelastic cross sections are probably quite small compared to the total absorption cross section.

"Scattering in"

The CH_2-C and D_2O-H_2O difference experiments were done in good geometry using a collimated beam 2 in. in diameter. Because the incident beam diverges slightly, a small portion if it (an estimated 7 percent) misses the detector unless scattered through the appropriate angle upon traversing the scatterer. However, due to the very small solid angle subtended by the detector, this effect contributes less than 0.5 percent to the observed counting rate for a typical carbon sample and is thus negligible.

In the transmission measurements of Be through U, a 1-in. collimated beam was used so that the entire unattenuated beam strikes the detector. Hence there is no scattering in effect.

Finite Scatterer Thickness

In the poor geometry measurements, the thickness, t, of the scattering sample is an appreciable fraction ($\sim\frac{1}{2}$) of the distance, l, from the center of the sample to the detector. Therefore, the half-angle θ, for collection is poorly defined. To correct the observed values of transmission to the idealized case of zero scatterer thickness and perfectly defined geometry, an approximate diffraction angular distribution is suitably averaged over the thickness, t, of the scatterer. The magnitude of this correction to the observed transmission is less than 0.6 percent in all cases and has been neglected. The effect is small for two reasons: (1) the integral angular distribution in bad geometry is a slowly varying function of θ; and (2) since the distance l is measured from the center of the sample, the correction is second order in (t/l).

Sample Dimensions and Impurities

The samples of polyethylene were molded from high purity commercial powder. The samples chosen are free from air bubbles and the measured density is 0.922 ± 0.001 g/cm^3. The carbon samples are blocks of reactor-grade graphite of extreme purity. The thickness in grams per cm^2 was measured to within ±0.5 percent. This uncertainty can introduce an error of at most 0.25 percent of the carbon cross section or ±0.9 mb.

The matched samples of heavy water—ordinary water are believed to contain negligible impurities and the thicknesses are known to 0.5 percent. The corresponding uncertainty in the "*n-n*" cross section is ±1.0 mb.

The samples of the eight elements, Be—U, were carefully weighed and measured so that the thickness in grams/cm^2 is known to within 0.5 percent. The effect of possible impurities is believed to be negligible in all cases.

Summary and Treatment of Error

In the measurement of the hydrogen and deuterium cross sections the dominant error arises from the random fluctuations. The standard deviations in the cross sections are listed in Table I. A minor correction is made for background.

The errors in measuring the transmissions of the elements Be—U consist of:

(a) An error due to random fluctuation which is taken is taken as 1.6 times the expected standard deviation due to statistics only.

(b) An uncertainty of 1 percent to include the effects of background, charged particles, and possible rate effects.

(c) An uncertainty in the correction for directionality of the telescope. This uncertainty is difficult to estimate. It is taken, somewhat arbitrarily, as ±20 percent of the correction itself. The contributions from (a), (b), and (c) are combined as random errors. The resultant errors in cross section are listed in Table III.

It should be noted that the uncertainties in the absorption cross sections do *not* include the possible effect of:

(d) Detection of neutral secondaries from inelastic processes. The estimates previously given in this section are probably upper limits to this effect.

(e) Uncertainties in the theoretical angular distributions that are used in Sec. IV(a) to interpret the measured cross sections.

IV. OPTICAL MODEL ANALYSIS OF THE NUCLEAR CROSS SECTIONS

The present experiment yields three quantities for each nucleus: the total nuclear cross section σ_T, the absorption cross section σ_a, and a measure of the width of the diffraction scattering. According to the optical model approximation, σ_a is a function of the nuclear radius R, and the absorption constant K; while σ_T and the shape of the diffraction curve are functions of R, K, and k_1, the increment in the wave number inside the nucleus. In addition, σ_a, σ_T, and the diffraction pattern, depend on the assumed nuclear density distribution (which may contain more than one radial parameter), and on the wave number k, of the incident neutrons. Furthermore, it has been recently shown[22–24] that a nuclear spin-orbit potential is present, which influences the diffraction part of the total cross section in the 200- to 400-Mev region.

It is clear that all of the pertinent parameters cannot be independently deduced from the three measured quantities. Since the incident neutrons are not monoenergetic, no information can be obtained about the nuclear density distribution. Rather, the width of the diffraction curve, is used to determine the effective mean neutron energy as detected by the counter telescope. Substituting the measured values of the free nucleon-nucleon cross sections into the definition of K, σ_a becomes a function of R only. Hence the value of σ_a will determine the nuclear radius parameter for an assumed nuclear density distribution.

(a) Uniform Density Model

The uniform density model has the virtue of simplicity, although it is certainly no more than a first approximation. The pertinent formulas as given by Fernbach, Serber, and Taylor,[14] for a sphere of radius R, are:

$$\sigma_a=2\pi\int_0^R(1-u^2)rdr=\pi R^2\left\{1-\frac{(1-2KR)e^{-2KR}}{2K^2R^2}\right\}, \quad (1)$$

$$\sigma_T=\sigma_a+\sigma_d=\sigma_a+2\pi\int_0^R|(1-u)|^2rdr, \quad (2)$$

where σ_d is the total diffraction scattering, and u is the transmitted wave amplitude at impact parameter r.

$$u=\exp\{-(K+ik_1)(R^2-r^2)^{\frac{1}{2}}\}. \quad (3)$$

The quantities K and k_1 can be expressed in terms of the average nucleon-nucleon cross section, $\bar{\sigma}$, and the nucleon-nucleon forward scattering amplitude, $f(0)$:

$$K=\frac{A\bar{\sigma}}{(4/3)\pi R^3} \quad \text{or} \quad KR=\frac{A\bar{\sigma}}{(4/3)\pi R^2}, \quad (4)$$

$$k_1=(2\pi\rho/k)\,\mathrm{Re}\,f(0), \quad (5)$$

where ρ is the nuclear density. The elastic differential scattering cross section is given by

$$\frac{d\sigma_d}{d\Omega}=k^2\left|\int_0^R(1-u)J_0(kr\sin\theta)rdr\right|^2. \quad (6)$$

For $KR>1$, $d\sigma_d/d\Omega$ is very similar in angular distribution to the diffraction scattering from a cylinder, namely

$$\frac{d\sigma_d}{d\Omega}\sim\left[\frac{J_1(kR\sin\theta)}{\sin\theta}\right]^2. \quad (7)$$

Finally we shall define the partially integrated differential cross section normalized to unity:

$$F(\theta)=\frac{1}{\sigma_d}\int_0^\theta\frac{d\sigma_d}{d\Omega}d\Omega. \quad (8)$$

$F(\theta)$ is quite insensitive to the values of KR and k_1/K. Its functional form depends almost exclusively on the parameter kR. Detailed numerical computations of $F(\theta)$ for a fixed R and for various values of k corresponding to energies from 1 to 2.2 Bev show that the values of $F(\theta)$ in the range 0.1 to 0.6 are independent of the spectrum of k values of the incident neutrons, and depend only on the average value of k, $\langle k\rangle$. In the Bev energy range, a linear average of k is equivalent to a linear average of energy. It can be shown that the following relationship is valid, independent of k_1 and K:

$$\langle k\rangle R\theta_{\frac{1}{2}}=1.7, \quad (9)$$

where $F(\theta_{\frac{1}{2}})=0.5$ defines $\theta_{\frac{1}{2}}$. The transmission measured at a given subtended angle θ determines a cross section $\sigma(\theta)$ given by

$$\sigma(\theta)=\sigma_a+[1-F(\theta)]\sigma_d. \quad (10)$$

If T_1 and T_2 denote the limiting transmissions in good and bad geometry [$F(\theta)=0$ and 1, respectively], then $\theta_{\frac{1}{2}}$ is determined by $T(\theta_{\frac{1}{2}})=(T_1T_2)^{\frac{1}{2}}$. Near T_1 and T_2, $F(\theta)$ is insensitive to the value of $\langle k\rangle R$. The angles $\theta=\theta_{\frac{1}{2}}$ are shown in Figs. 10, 11, and 12 for C, Cu, and Pb. By using the values of R deduced from σ_a for each element, $\langle k\rangle$ is deduced from Eq. (9). The results from the three experimental curves are consistent with the single value $\langle k\rangle=(10.2\pm1.4)\times10^{13}$ cm^{-1}. This corresponds to a mean effective neutron energy of 1.4 ± 0.2

[22] Oxley, Cartwright, and Rouvina, Phys. Rev. **93**, 806 (1954).
[23] Chamberlain, Segrè, Tripp, Wiegand, and Ypsilantis, Phys. Rev. **93**, 1430 (1954).
[24] Marshall, Marshall, and de Carvalho, Phys. Rev. **93**, 1431 (1954).

Bev. The solid curves shown in Figs. 10, 11, and 12 are theoretical curves obtained from Eq. (8) using this value of $\langle k \rangle$, as well as the measured values of σ_T and σ_a. Specifically, the curves are calculated for $KR=3$ and $k_1/K=0$.

The integral angular distribution of Eq. (8) describes single-diffraction scattering only. Multiple-diffraction scattering will introduce small changes in Eq. (10) as described in Appendix C. These corrections vanish at both small and large values of θ. They are only important in the intermediate angular region, that is, where $d\sigma_d/d\Omega$ has maximum curvature, e.g., 1.5° to 4° for Pb. This is the same region where the corrections for the directionality of the telescope and the effects of uncertainty in $\langle kR \rangle$ are largest. Hence this intermediate angular region is subject to considerable uncertainty, and is, therefore, not used in determining the values of σ_a and σ_d.

To determine σ_a and σ_d, Eq. (10) is averaged over the transmissions in good geometry (0.2° to 0.7°) and in poor geometry (6°–10°). The values of σ_a, σ_T, and σ_d for the eight elements Be—U are listed in the first three columns of Table III.

To determine the radius R from σ_a, we assume that $\bar{\sigma}$, the average nucleon-nucleon cross section for bound nucleons, is equal to the average n-p and n-n cross section for free nucleons. Equation (1) is then used to determine R from the experimental values of σ_a. Table III gives the values of K and R for $\bar{\sigma}=43$ mb, and also for a smaller value, $\bar{\sigma}=30$ mb. The values of R obtained for the heavy elements are quite insensitive to the variation in $\bar{\sigma}$, since the uniform sphere is fairly opaque, i.e., R is essentially equal to $[\sigma_a/\pi]^{\frac{1}{2}}$. The values of R are plotted *vs* $A^{\frac{1}{3}}$ in Fig. 13. For $\bar{\sigma}=43$ mb, the least

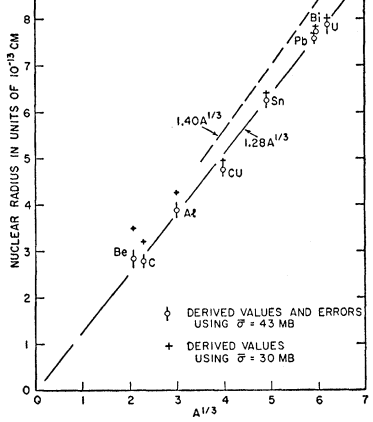

FIG. 13. Nuclear radius *vs* $A^{\frac{1}{3}}$ for the uniform density model, using two different values for $\bar{\sigma}$, the average nucleon-nucleon cross section in nuclear matter. The best straight line through the points and through the origin for $\sigma=43$ mb yields $R=(1.28\pm0.015)A^{\frac{1}{3}}\times10^{-13}$ cm. For comparison the curve $1.40A^{\frac{1}{3}}$ is shown.

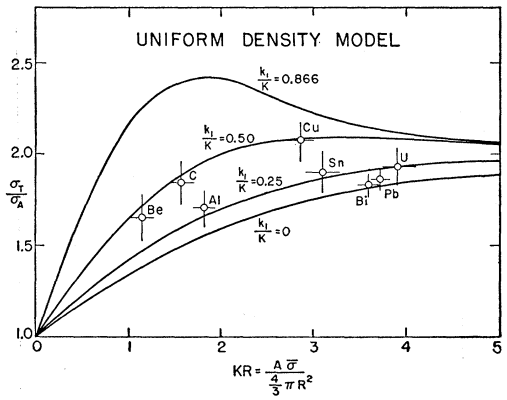

FIG. 14. Experimental points of σ_T/σ_a *versus* KR and the corresponding theoretical curves for various values of k_1/K using the uniform density model. R, K, and k_1 are the optical model parameters for a uniform sphere.

squares fit through the origin yields $R=(1.28\pm0.015)A^{\frac{1}{3}}\times10^{-13}$ cm. Having determined R and KR, the quantity (σ_T/σ_a), as determined by Eq. (2), is a function of k_1/K. In Fig. 14, theoretical curves of σ_T/σ_a *vs* KR are plotted for various values of k_1/K, together with the experimental values tabulated in Table III. The uncertainties are large, but it appears that the measured values are consistent with a single value of $k_1/K=0.3\pm0.1$ for all eight nuclei.

The uniform density interpretation is reasonably consistent in that (i) the nuclear density is constant for all the nuclei except possibly for beryllium, and (ii) a constant value of (k_1/K) crudely fits the data for all the nuclei. The significance of the derived values of R, k_1 and K is discussed in Sec. V.

(b) Gaussian Density Model

A similar analysis is carried through again by using the optical model but assuming a Gaussian density distribution. This distribution is chosen as an easily calculable extreme example of a smeared-out density distribution, and there are arguments based on the shell model which suggest that it may be a realistic one.[25] A normalized density of nucleons as given in Eq. (11) is assumed and the radius parameter, a, for each nucleus is then to be determined.

$$\rho(r)=\frac{A}{(a\sqrt{\pi})^3}\exp[-(r/a)^2]. \tag{11}$$

The path length t (in mean free paths) for impact parameter r is again Gaussian:

$$t(r)=2\int_0^\infty \rho([r^2+s^2]^{\frac{1}{2}})ds=(t_0)\exp[-(r/a)^2], \tag{12}$$

[25] M. Born and L. M. Yang, Proc. Phys. Soc. (London) **A64**, 632 (1951).

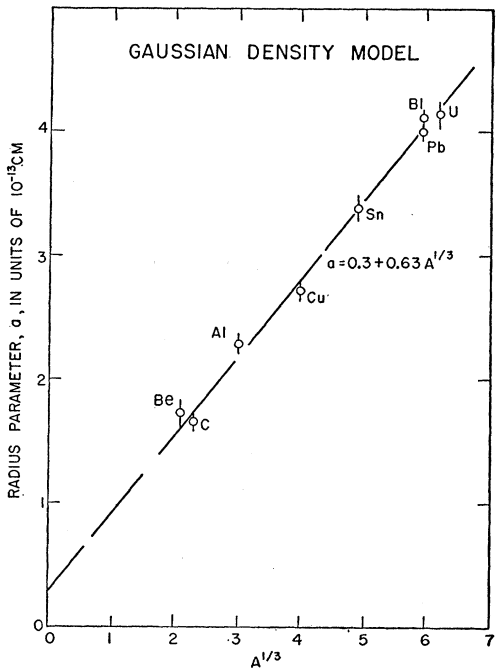

FIG. 15. Nuclear radius parameter a *versus* $A^{\frac{1}{3}}$ for the Gaussian density model, i.e., $\rho=\rho_0\exp[-(r/a)^2]$. The best straight line through the points is shown. The radii were determined from Eq. (13a) using $\bar{\sigma}=43$ mb.

where $t_0=A\bar{\sigma}/\pi a^2$. σ_a becomes

$$\sigma_a=2\pi\int_0^\infty rdr(1-e^{-t}),$$
$$\sigma_a=\pi a^2\{\gamma+\ln t_0-\mathrm{Ei}(-t_0)\}=\pi a^2 G(t_0), \tag{13}$$

where γ is Euler's constant (0.5772) and $\mathrm{Ei}(-t_0)$ is the exponential integral,

$$\mathrm{Ei}(-t_0)=\int_\infty^{t_0}(e^{-t}/t)dt.$$

To derive the values of the radius parameter a, Eq. (13) is rewritten in the form

$$\frac{\sigma_a}{A\bar{\sigma}}=\frac{1}{t_0}G(t_0). \tag{13a}$$

For an assumed $\bar{\sigma}$, this equation is solved graphically for t_0, which then yields the value of a. The results calculated on the assumption that $\bar{\sigma}=43$ mb are plotted in Fig. 15. The best fit yields $a=0.3+0.63A^{\frac{1}{3}}$.

To obtain a useful express for σ_T/σ_a as a function of t_0 and k_1/K, we consider:

$$\sigma_T(t_0,k_1/K)=2\pi\int_0^\infty rdr\{|1-u|^2+1-u^2\},$$
$$\sigma_T=4\pi\int_0^\infty rdr\{1-e^{-t/2}\}$$
$$+4\pi\int_0^\infty rdr[1-\cos(k_1t/K)]e^{-t/2}, \tag{14}$$

where the first integral is $\sigma_T(t_0,0)$ and is recognized as:

$$\sigma_T(t_0,0)=2\pi a^2G(t_0/2). \tag{15}$$

The second integral which contains the dependence on k_1/K is given to a good approximation, for $t_0\geq 5$ and $k_1/K\geq 0.6$, by:

$$4\pi\int_0^\infty rdr[1-\cos(k_1t/K)]e^{-t/2}$$
$$=2\pi a^2\int_0^{t_0}\frac{dt}{t}[1-\cos(k_1t/K)]e^{-t/2}$$
$$\cong\pi a^2\{\ln[1+4(k_1/K)^2]+2\,\mathrm{Ei}(-t_0/2)\}, \tag{16}$$

and for $k_1t_0/K<1$ by:

$$\cong 4\pi a^2(k_1/K)^2\{1-(1+\tfrac{1}{2}t_0)e^{-t_0/2}\}.$$

With these results, σ_T/σ_a is plotted as a function of t_0 for $k_1/K=0$, 0.6 and 1.0 in Fig. 16. A value of $k_1/K=0.6\pm0.2$ fits the results for all eight nuclei. It is clear that to the accuracy of this experiment the Gaussian density model and the uniform density model fit the data equally well.

V. DISCUSSION AND CONCLUSIONS

(a) Neutron Energy Considerations

The fact that a broad energy spectrum must be employed in this experiment is probably not as serious an objection to the method as it might appear at first sight, since the expectation is that the cross sections of interest are not strongly energy-dependent in the energy range from about 1 to 2.2 Bev. (This appears to be borne out by recent results for the total p-p and p-d cross sections.)[26]

To determine whether the estimate of mean energy depends critically on the nuclear model, a numerical calculation was made of the diffraction angular dis-

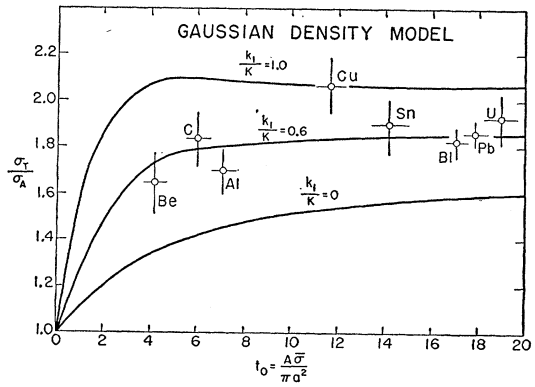

FIG. 16. Experimental points of σ_T/σ_a *versus* t_0 and the corresponding theoretical curves for various values of k_1/K. t_0 is an optical model parameter for a Gaussian density distribution that is analogous to the quantity KR for a uniform-sphere distribution.

[26] Chen, Leavitt, and Shapiro (private communication).

tribution expected for a Gaussian density model. The Gaussian model calculation for lead, using the radius parameter $a=4.0\times10^{-13}$ cm, derived in Sec. IV, yields an angular distribution for the first lobe of the diffraction pattern almost indistinguishable from the uniform model calculation. The second lobe is also present but reduced to about one-third the value for the uniform model. The important point is that the angular half-width of the diffraction pattern for lead is practically the same for Gaussian and uniform density models fitted to the same absorption cross section. Therefore, the mean energy estimate of 1.4±0.2 Bev is insensitive to the choice of nuclear model.

A study has been made by the Brookhaven Cloud Chamber Group[27] of energetic three-pronged events produced in a hydrogen-filled chamber in the forward neutron beam. Of some 150 events observed, about 100 are of the type $n+p\rightarrow n+p+\pi^+ +\pi^-$; the remaining events are $n+p\rightarrow p+p+\pi^-$ and $n+p\rightarrow p+p+\pi^- +\pi^0$. The mean primary energy for these three types of events is observed to be 1.7 Bev. A significant comparison of this mean value with the value 1.4 Bev from the present experiment is not possible, since neither the energy dependence of the meson production process nor the energy response of the neutron detector is known. However, it is certainly plausible that the three-prong events, being mainly two-meson production events, weight the higher energies more on the average than does the neutron telescope detector. There appears to be a suppression of one-meson n-p production events of the type $pp\pi^-$, which can be understood if the mesons are made predominantly in $T=\frac{3}{2}$ states.[28] There is no experimental evidence for any peaking of the neutron energy spectrum near 2.2 Bev, corresponding to elastic charge exchange scattering.

The fairly low mean neutron energy of 1.4 Bev for neutrons emerging at 1° to the incident proton beam implies that most of the neutrons arise from strongly inelastic events, such as two-meson production events. This conclusion agrees with the experiments of Lindenbaum and Yuan,[29] which show that the mesons emerging at 32° to the direction of the incident 2.2-Bev protons predominantly arise in two-meson production processes.

(b) Nucleon-Nucleon Cross Sections

A comparison of the 1.4-Bev hydrogen and deuterium total cross sections (42 mb and 85 mb, respectively) with previous measurements at lower energies is shown in Fig. 17. A large increase in the total cross sections is apparent. This figure includes an indication of the total p-p cross sections,[30] including the recent Brookhaven measurements[31] from 0.4 to 1.5 Bev which show in detail how the cross section changes with energy. The p-p cross section at 1.4 Bev is about 48 mb. Charge symmetry of nuclear forces implies an equal n-n total cross section. On the other hand, our measured $[(n,d)-(n,p)]$ cross section at 1.4 Bev is 42 mb. This discrepancy suggests that even at these high energies one cannot treat the deuteron total cross section as a simple sum of the neutron and proton total cross sections. This effect is further confirmed by the fact that the $[(p,d)-(p,p)]$ total cross section[31] is again smaller than the (n,p) total cross section at 1.4 Bev by 8±2 mb. Of course, these comparisons would be more precise if the neutron beam were monoenergetic, but the essential flatness of the p-p cross section from 0.8 to 2 Bev makes these discrepancies appear to be significant. A similar effect is indicated by a comparison of the (π^+,p) and $[(\pi^-,d)-(\pi^-,p)]$ total cross sections in the 1-Bev region,[32] and at 170 Mev.[33] On the other hand, there is no evidence for a difference between the (n,d) and the $(n,p)+(p,p)$ total cross sections at 410 Mev.[10]

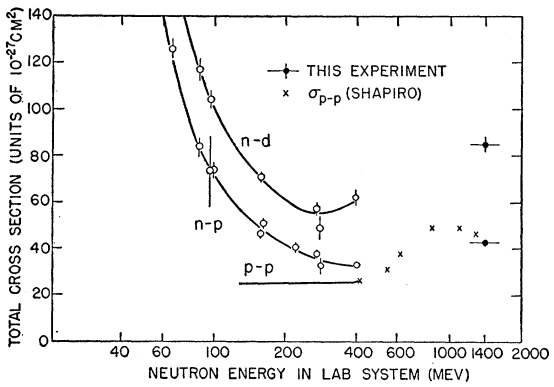

FIG. 17. Total n-p and n-d cross sections. The previously published data (see references 1–12) are indicated with open circles. An indication of the p-p total cross sections (see reference 30) is given, including the recent Brookhaven results (see reference 31).

A theoretical interpretation of the (n,d) cross section is a formidable problem. A simple addition of the elementary free nucleon cross sections may fail for many reasons, such as: (1) coherent elastic scattering from the two nucleons causing interference effects, (2) effects of the Pauli principle in excluding some final states, (3) shielding of one nucleon by the other and (4) three-body interactions. Gluckstern and Bethe[34] and Chew[35] have written several papers on the problem

[27] Fowler, Shutt, Thorndike, and Whittemore, Phys. Rev. **95**, 1026 (1954).
[28] D. C. Peaslee, Phys. Rev. **94**, 1085 (1954); **95**, 1580 (1954).
[29] S. J. Lindenbaum and L. C. L. Yuan, Phys. Rev. **95**, 638 (1954).
[30] The total p-p cross section from 150 to 400 Mev is consistent with a constant value about 25 mb. For example, see the work of H. de Carvalho, Phys. Rev. **96**, 398 (1954). Chamberlain, Pettengill, Segrè, and Wiegand, Phys. Rev. **93**, 1424 (1954); Marshall, Marshall, and Nedzel, Phys. Rev. **85**, 416 (1952); and Sutton, Fields, Fox, Kane, Mott, and Stallwood, Phys. Rev. **97**, 783 (1955).
[31] Shapiro, Leavitt, and Chen, Phys. Rev. **95**, 663 (1954).
[32] Cool, Madansky, and Piccioni, Phys. Rev. **93**, 637 (1954).
[33] Ashkin, Blaser, Feiner, Gorman, and Stern, Phys. Rev. **96**, 1104 (1954).
[34] R. L. Gluckstern and H. A. Bethe, Phys. Rev. **81**, 761 (1951).
[35] G. Chew, Phys. Rev. **74**, 809 (1948); **80**, 196 (1950); **84**, 710 (1951).

at lower energies where only elastic nucleon-nucleon scattering is present. The first authors interpret the 90-Mev *n-d* total cross sections by using a static potential and the Born approximation (in a way that is more or less equivalent to the impulse approximation). They conclude that simple additivity may fail by about 20 percent at that energy; furthermore, the (*n-d*) total cross section may be greater or less than the sum (*n-n*) plus (*n-p*), depending on the exchange character assumed for the *n-n* interaction. They note that the failure of additivity is more marked for the elastic *n-d* cross section which is almost half the total at 90 Mev. They estimate that the elastic part should remain roughly a constant fraction of the total at higher energies. At 1.4 Bev one might expect similar considerations to hold for the elastic parts of the *n-p* and *n-n* cross sections, since they involve small momentum transfers. On the other hand, the meson-production parts of the cross sections are probably more nearly additive, since they involve much larger momentum transfers.

It is this last point, that is, the presence of an inelastic nucleon-nucleon interaction (meson production involving large momentum transfer), that makes the identification of the $\bar{\sigma}$ of the optical model with the average "free" nucleon-nucleon cross section seem reasonable at 1.4 Bev. If it is true that only the elastic part of the nucleon-nucleon cross section is influenced appreciably by the Pauli principle acting inside a nucleus, then the percentage difference between $\bar{\sigma}$ and the free cross sections will be reduced in the ratio of the nucleon-nucleon elastic to total cross sections.

(c) Optical Model Parameters K and k_1

The analysis of Sec. IV in terms of the uniform density model leads to the following average values of the optical model parameters:

$$K=0.49\times10^{13}\ \text{cm}^{-1},$$
$$k_1=(0.15\pm0.05)\times10^{13}\ \text{cm}^{-1}. \tag{17}$$

Both of these values are considerably higher than those used to fit the data in the 300-Mev region according to the analysis of Taylor.[36] The increase in K reflects the increased nucleon-nucleon cross section and an increased nuclear density. No new information is contained in the parameter K since it is completely determined by the assumed value of $\bar{\sigma}$ and the deduced value for the nuclear radius. For the light elements, K is a sensitive function of the value assumed for $\bar{\sigma}$.

The constant k_1 does yield some additional information, since it is related to the real part of the average nucleon-nucleon forward scattering amplitude as given by Eq. (18).

$$k_1=(2\pi\rho/k)\ \text{Re}f(0), \tag{18}$$

where ρ is the nucleon density. The value of k_1 given in Eq. (17) corresponds to $\text{Re}f(0)=(2.1\pm0.7)\times10^{-13}$ cm. This implies a minimum value for the forward elastic neutron-nucleon cross section of the order of 44_{-24}^{+34} mb/steradian. This high value implies that the elastic nucleon-nucleon scattering is strongly peaked in the forward direction. For the Gaussian model the same calculation gives a value twice as large for $\text{Re}f(0)$. It has been customary in the lower-energy regions to relate the constant k_1 to an average nuclear potential. At these energies it is questionable whether an "average nuclear potential" has significance. In any case, applying the relativistic relation

$$k_1=\bar{V}/\hbar c\beta, \tag{19}$$

leads to an average potential $\bar{V}=26\pm9$ Mev.

(d) Nuclear Radii

The data of this experiment can be fitted to a good approximation with a uniform density model having radii given by $R=r_0A^{\frac{1}{3}}$ with $r_0=1.28$ in units of 10^{-13} cm.[37]

While the literature on neutron-nuclei cross sections above 40 Mev is extensive, the emphasis has been largely on transmission experiments in good geometry to measure total cross sections. In several cases, inelastic cross sections have been measured in bad geometry and, in a few cases, differential scattering experiments have been done. For comparison, we cite some of the uniform density radii obtained from these investigations.

Cook *et al.*[1] give the value $r_0=1.37$ from an analysis of the 14- and 25-Mev neutron data; Fernbach, Serber, and Taylor[14] find that the 90-Mev neutron data can be consistently fitted with the same value. Taylor[36] has interpreted the 50- and 150-Mev neutron data as well as Nedzel's 400-Mev data[10] to yield values of r_0 from 1.37 for lead to 1.54 for carbon.

Our method of analysis, using the absorption cross sections measured by Ball[9] at 300 Mev and assuming $\bar{\sigma}=27$ mb, yields $r_0=1.31$ for lead and 1.52 for carbon. Gatha and Riddell[38] have used the 340-Mev proton data of Richardson *et al.*[39] to obtain $r_0=1.25$. The recent work of Chen[15] with 860-Mev protons leads to the value $r_0=1.25$. The radii reduced from our data are believed to be consistent with most of the previous nuclear experiments. The apparent inconsistencies, particularly for the radii of light nuclei, are probably not outside the sum of the experimental errors and the uncertainties in the theoretical interpretations.

It is of interest to compare the nuclear proton distribution radii found from electromagnetic interactions with the nuclear radii found here. Since the various

[36] T. Taylor, Phys. Rev. **92**, 831 (1953).

[37] A least squares fit of the nuclear radii, assuming the relation $R=b+r_0A^{\frac{1}{3}}$ gives $R=0.16+1.31A^{\frac{1}{3}}$. For $b\neq0$, the coefficient r_0 deviates from the value 1.28, which holds for $b=0$, as $r_0=1.28+0.21b$.

[38] K. M. Gatha and R. J. Riddell, Phys. Rev. **86**, 1035 (1952).

[39] Richardson, Ball, Leith, and Mayer, Phys. Rev. **83**, 859 (1951).

measurements involve different radial averages the assumed shape of the density function can play an important role in such a comparison. For example, the analysis of Hill and Ford[40] of the μ-mesonic x-ray data of Fitch and Rainwater[41] yields, for lead, a uniform density model radius $R=6.95$ (corresponding to $r_0=1.17$) while for a Gaussian model, the radial parameter $a=4.62$ results. The results for lead in the present experiment are $R=7.55$ (uniform model) and $a=4.0$ (Gaussian model). Hence for the uniform model one obtains a smaller "electromagnetic" radius than the "neutron absorption" radius, while for the Gaussian model the *situation is reversed.* This is a consequence of the fact that the μ-mesonic x-ray data yields a parameter approximately proportional to $\langle r^{0.5}\rangle$ for heavy elements,[40] while the neutron absorption data yields a parameter that weights the tail of the density distribution much more heavily. On the other hand, the high-energy electron scattering data of Hofstadter *et al.*,[17] as interpreted by Ravenhall and Yennie,[42] show that a smoothed uniform density function, which lies in between the extreme uniform and Gaussian functions, is required. Fitting such a density function to our neutron absorption data for the heavy elements, R. Williams, in the following paper, finds radial parameters that agree quite well with the electron scattering parameters. Apparently a comparison of these two sets of data does not necessitate a nuclear radius that is 10–20 percent larger than the electromagnetic radius for a smoothed-out nuclear density function.

Comparison with Cosmic-Ray Results

The cosmic-ray data on the absorption of the high-energy nucleonic component provides information on the absorption cross sections for much higher energies than those used in this experiment. Table IV presents some of the cosmic-ray data for comparison with our results. There seems good evidence that the absorption length decreases with increasing primary energy.[11] In particular, λ_a becomes shorter than the value of λ_{geom} given by the present data. This result cannot be understood in terms of a uniform-density model but might be explained by a "long-tailed" density distribution if the nucleon-nucleon cross sections increase with energy. Williams has given such an explanation in a succeeding paper as well as a more critical survey of the subject.

The authors wish to express their appreciation to Professor R. Williams for several stimulating discussions, to the several members of the counter groups at the Cosmotron for the loan of special absorbers and for their helpful and sympathetic discussions, and to the members of the operating crew and staff of the Cosmotron for their unstinting cooperation in all phases of this work. We also wish to thank Mildred Widgoff and F. F. Chen, C. Leavitt, and A. M. Shapiro for making available their results prior to publication.

TABLE IV. Comparison with cosmic-ray data.

1. Present experiment	Carbon	Lead
λ_a	99±5 g/cm²	199±5 g/cm²
λ_{geom}	(83±8)	(191±6)

2. Values of λ_a from cosmic-ray data on absorption of N-rays

	Carbon	Lead	Multiplicity of detected event
Walker[a]		180±10	$N=4$, 5 penetrating 230 g/cm²
		147±10	$N>7$, 230 g/cm²
Walker, Walker and Greisen[b]			
charged primaries	82±8	157±12	$N>7$, penetrating
neutral primaries	80±7	164±15	230 g/cm² Pb
Boehmer and Bridge[c]			
neutral primaries	110	220	$N\geq 2$
Sitte[d]			$N\geq 3$ penetrating
charged primaries		196±13	100 g/cm² Pb
		162±10	200 g/cm² Pb

[a] W. D. Walker, Phys. Rev. **77**, 686 (1950).
[b] Walker, Walker, and Greisen, Phys. Rev. **80**, 546 (1950).
[c] H. W. Boehmer and H. S. Bridge, Phys. Rev. **82**, 306 (1951); Rossi, reference 11.
[d] K. Sitte, Phys. Rev. **78**, 714 (1950).

APPENDIX A

Directionality Correction

The correction for the variation of detection efficiency with angle is calculated from the idealized model of the detector shown in Fig. 18. Consider a uniform parallel beam of circular cross section (radius P) incident on a thin scatterer.

A typical particle incident on the scatterer at A (a distance ρ from the axis) is scattered through the space angle θ (and azimuthal angle β) and strikes the radiator at B giving rise to a distribution of charged secondaries in the forward direction with axial symmetry about the line AB. The probability that one of these secondaries shall discharge the last counter then depends only on the angle φ between AB and BC, where C is the center of the last counter. Summing the contributions to the observed counting rate from all elements of the beam

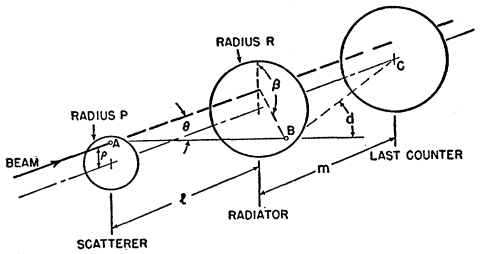

FIG. 18. Geometrical model used to calculate the correction factor C_1, due to the variation of detector response with incident neutron angle.

[40] D. L. Hill and K. W. Ford, Phys. Rev. **94**, 1617 (1954).
[41] V. L. Fitch and J. Rainwater, Phys. Rev. **92**, 789 (1953).
[42] D. G. Ravenhall and D. R. Yennie, Phys. Rev. **96**, 239 (1954).

cross section and all scattering angles up to ξ leads to the expression:

$$C_{\text{in}}(\xi)=n_0e^{-t/\lambda_T}\frac{2}{P^2}\int_0^P\rho d\rho g(\rho/m)+n_0S\frac{2}{P^2}\int_0^P\rho d\rho\int_0^\xi\psi(\theta)\bar{g}(\varphi)d\theta, \quad \text{(A-1)}$$

$$C_{\text{out}}=n_0\frac{2}{P^2}\int_0^P\rho d\rho g(\rho/m), \quad \text{(A-2)}$$

where $C_{\text{in}}(\xi)$ = counting rate with scatterer in and detector subtending nominal half-angle ξ, $\xi=R/l$ for small angles, C_{out} = counting rate with scatterer out, $g(\varphi)$ = probability of detection of neutron entering radiator at some point B at angle φ to the line BC, n_0 = flux of neutrons incident on scatterer, S = probability that a neutron is scattered and emerges from the scatterer, and $\psi(\theta)$ = normalized angular distribution of scattered particles, i.e., $\int_0^\pi\psi(\theta)d\theta=1$. For small angles:

$$\varphi^2=\left(1+\frac{l}{m}\right)^2\theta^2+\left(\frac{\rho}{m}\right)^2+2\frac{\rho}{m}\left(1+\frac{l}{m}\right)\theta\cos\beta, \quad \text{(A-3)}$$

and $\bar{g}$ is the average of g over all values of β. In short, Eq. (A-1) represents an average of the efficiency g over (a) the angular distribution ψ, (b) the azimuth angle β, and (c) the cross section of the incident beam. It is expected to be valid only in the poor geometry limit since it contains the assumption that essentially all of the scattered particles strike the radiator. Only in this limit, is it proper to average g over all values of β and use the nominal angle ξ for the upper limit of the average (a) over the angular distribution. To be exact, this upper limit depends also on ρ and β but has a mean value of ξ. In the poor geometry limit the average (a) is insensitive to the upper limit.

The observed transmission T can now be written as:

$$T(\xi)=C_{\text{in}}/C_{\text{out}}=e^{-t/\lambda_T}+S\int\rho d\rho\int\psi\bar{g}d\theta\Big/\int\rho d\rho g. \quad \text{(A-4)}$$

The function g is expanded in even powers of φ according to Eq. (A-5). Then by using relation (A-3), the average over β is easily taken:

$$g(\varphi)=g_0(1-a\varphi^2+b\varphi^4+\cdots). \quad \text{(A-5)}$$

After the integration over ρ and rearrangement [noting that $T(0)=e^{-t/\lambda_T}$], Eq. (A-4) becomes:

$$S\int_0^\xi\psi d\theta=[T(\xi)-T(0)]C_1=[T(\xi)-T(0)]\times\left\{1-\frac{(1+R/m\xi)^2[a-2b(P/m)^2]\langle\theta^2\rangle_\xi-b(1+R/m\xi)^4\langle\theta^4\rangle_\xi}{1-\frac{1}{2}a(P/m)^2+\frac{1}{3}b(P/m)^4}\right\}^{-1}, \quad \text{(A-6)}$$

in which

$$\langle\theta^2\rangle_\xi=\int_0^\xi\theta^2\psi d\theta\Big/\int_0^\xi\psi d\theta, \text{ etc.} \quad \text{(A-7)}$$

This expresses the "true" integral angular distribution $S\int_0^\xi\psi d\theta$ in terms of the observed transmissions $T(\xi)-T(0)$, with a correction factor depending on the moments of the distribution, the angle ξ, and the constants a, b which enter in the function g. The function g was determined empirically by observing the relative counting rate as the detector is rotated, relative to the collimated beam, with the radiator remaining fixed in the beam. The result is the angular distribution of penetrating charged secondaries from aluminum as shown in Fig. 7. The distribution is very well fitted for angles up to 15° by a polynomial of the form (A-5) with the constants: $a=6.42\times10^{-3}$, $b=1.70\times10^{-5}$ (for φ in degrees).

To evaluate the moments, $\langle\theta^2\rangle_\xi$ and $\langle\theta^4\rangle_\xi$, which enter the correction term, an approximate angular distribution is taken of the form:

$$\psi_1=(\theta/\eta)\exp(-\theta^2/2\eta^2), \quad 0\leq\theta\leq3\eta \quad \text{(A-8a)}$$

$$\psi_2=0.44(\eta/\theta)^2, \quad \theta>3\eta \quad \text{(A-8b)}$$

$$\eta=86.0/kR \text{ (in degrees)}. \quad \text{(A-8c)}$$

For all elements, ψ_1 is a good approximation to the first lobe of the diffraction pattern predicted by the optical model if the angle η at which the maximum occurs, is chosen according to (A-8c). The quantity ψ_2 approximates the "tail" of the pattern with the maxima and minima smoothed out; the normalization constant is chosen so that about 87 percent of the scattering is included in the first lobe. With this choice of ψ_1 and ψ_2, the moments are calculated. Inserting these in Eq. (A-7), one obtains the factor, C_1, by which the observed value of $T(\xi)-T(0)$ must be multiplied. Figure 19 displays C_1 *versus* ξ for several values of the parameter

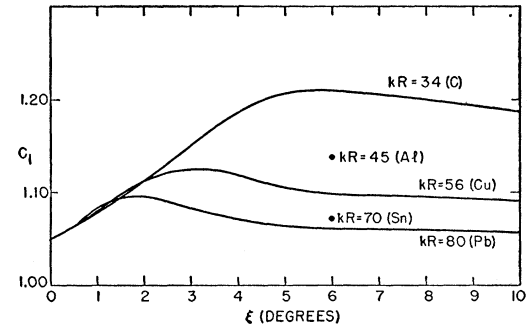

FIG. 19. Correction factor C_1 *versus* angle, ξ, subtended by the detector at the scatterer for several values of the parameter kR. C_1 is the factor by which the observed transmission is multiplied to obtain the corrected transmission. The correction varies from 6 percent of σ_a in lead to 24 percent of σ_a in carbon.

kR. The value of C_1 in the good geometry limit, $\xi \to 0$, is gotten by comparing the average efficiency for detecting the scattered particles, which are in this case parallel to the axis and uniform over the $2\frac{1}{2}$-in. aperture, with the efficiency for the unattenuated beam, which is parallel and uniform over a 1-in. diameter circle.

$$\lim_{\xi\to 0} C_1 = \int_0^P \rho d\rho g \Big/ \int_0^R \rho d\rho g = 1.05. \qquad \text{(A-9)}$$

The absolute correction to the observed transmission vanishes in this limit since $T(\xi)-T(0)$ goes to zero.

It is noted that the effect on the correction of averaging over finite beam size is negligible; that is, if $P \to 0$ in Eq. (A-6) the correction is practically unchanged. In other words, the correction in poor geometry is necessary primarily because of the *divergence* of the scattered particles which are collected.

When the detector was modified by replacing the third and fourth counters with 4-in. and 6-in. diameter counters, the angular distribution, g, was remeasured and found to be about 30 percent broader than that for the narrow-angle telescope. The magnitude of the correction (that is, C_1-1) was recomputed and is about 30 percent smaller for the modified telescope.

APPENDIX B

Finite Beam Size Correction

Because of the diameter of the beam (1 in.) is not negligible compared to the aperture of the detector ($2\frac{1}{2}$ in.) the angle subtended by the detector is not well defined. To relate the observed transmission to the ideal case of zero beam width a correction is made using the simplified model of Fig. 20. Consider a uniform parallel beam of circular cross section incident on the scatterer. The probability, h, that a particle scattered at A shall enter the detector is a function of ρ, θ, R, and l. Picturing this scattering in the plane of the detector, it is seen that $h=\beta_1/\pi$, where β_1 is defined, as shown, by $l\theta/R$ and ρ/R. To make this correction it is assumed that the detection efficiency is uniform and independent of θ, since these effects were treated independently in Appendix A.

Using the notation of Appendix A, the observed counting rates can be expressed as:

$$C_{\text{in}}(\xi) = n_0 e^{-t/\lambda T} + n_0 S \frac{2}{P^2} \int_0^P \rho d\rho \int_0^\pi \psi(\theta) h\left(\frac{\rho}{R}, \frac{l\theta}{R}\right) d\theta, \qquad \text{(B-1)}$$

$$C_{\text{out}} = n_0.$$

Hence

$$T(\xi) - T(0) = S \frac{2}{P^2} \int \rho d\rho \int \psi(\theta) h\left(\frac{\rho}{R}, \frac{\theta}{\xi}\right) d\theta, \qquad \text{(B-2)}$$

where $\xi = R/l$. Solving the triangle of Fig. 20 for β_1,

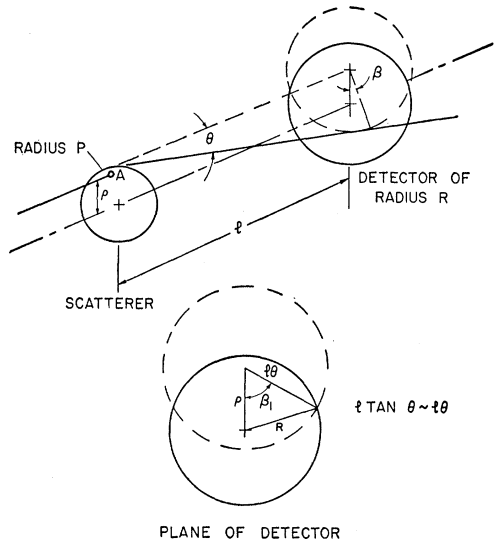

FIG. 20. Geometrical model used to calculate the correction factor C_2, due to the finite size of the incident neutron beam.

we obtain

$$\tan^2\left(\frac{\beta_1}{2}\right) = \frac{(1-\theta/\xi+\rho/R)(1+\theta/\xi-\rho/R)}{(1+\theta/\xi+\rho/R)(-1+\theta/\xi+\rho/R)},$$

$$h = \beta_1/\pi, \qquad \text{(B-3)}$$

from which h was calculated for several values of ρ/R. The function h is well approximated by straight line segments according to:

$$h = \begin{cases} 1, & (\theta/\xi) < (1-\rho/R) \\ \frac{1}{2} - \frac{1}{2\pi}\frac{\rho}{R} - \frac{1}{\pi}\frac{R}{\rho}\left(\frac{\theta}{\xi} - 1\right), & \\ & [1-(\rho/R)] \le (\theta/\xi) \le 1+(\rho/R) \\ 0, & (\theta/\xi) > 1+(\rho/R). \end{cases} \qquad \text{(B-4)}$$

The integral of Eq. (B-2) is then rewritten as

$$S\left(\frac{2}{P^2}\right)\int_0^P \rho d\rho \left\{ \int_0^\xi \psi d\theta - \underbrace{\int_{\xi-(\rho/l)}^{\xi} \psi d\theta}_{\text{I}} + \underbrace{\int_{\xi-(\rho/l)}^{\xi+(\rho/l)} \psi h d\theta}_{\text{II}} \right\}.$$

To evaluate I and II, $\psi(\theta)$ is expanded in Taylor series about $\theta=\xi$. The approximation of (B-4) is used for $h(\rho/R,\theta/\xi)$ and the integration performed. Rearranging (B-2) and using the results of integration, we have

$$S\int_0^\xi \psi d\theta = [T(\xi)-T(0)]\left\{1 + A \Big/ \int_0^\xi \psi d\theta\right\}^{-1} = [T(\xi)-T(0)]\times C_2, \qquad \text{(B-5)}$$

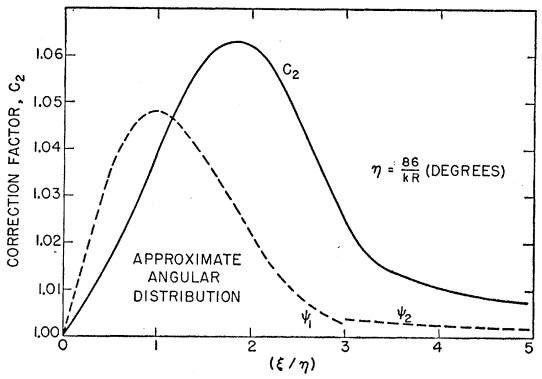

FIG. 21. Correction factor C_2 *versus* the ratio ξ/η. ξ is the angle subtended by the detector at the scatterer and $\eta=86/kR$, is the parameter used in the functions ψ_1 and ψ_2, defined by Eqs. (A-8a) and (A-8b), which approximate a diffraction pattern with the maxima and minima smoothed out. The functions ψ_1 and ψ_2, used to calculate corrections C_1 and C_2 are given by the dotted curves above.

with

$$A(\xi)=\sum_{n\ \text{even}}\frac{-2}{\pi(n+4)}\left(\frac{P}{R}\right)^{n+2}\frac{\xi^{n+1}\psi^{(n)}}{(n+1)!}$$
$$+\sum_{n\ \text{odd}}\left\{\frac{-4(n+1)}{\pi}+2(n+1)\right\}\left(\frac{P}{R}\right)^{n+1}\times\frac{\xi^{n+1}\psi^{(n)}}{(n+3)!},$$

where $\psi^{(n)}$ is the nth derivative of ψ evaluated at ξ. This expresses the true integral angular distribution in terms of the observed value $T(\xi)-T(0)$ and a correction factor C_2 which depends upon ψ and its derivatives at ξ. Assuming the approximate angular distributions of Appendix A and inserting the value $(P/R)=0.4$, it is found that the series for $A(\xi)$ converges rapidly with significant contributions only from terms in ψ and ψ'. To the extent that the *shape* of the angular distribution is the same for each element, the same correction C_2 applies for each element at corresponding points in the diffraction pattern. The quantity C_2 is plotted as a function of θ/η in Fig. 21; the scale factor η is given by $\eta=(86.0)/kR$ degrees according to (A-8c). The approximate angular distribution of Eqs. (A-8a) and (A-8b) is also included in the figure.

APPENDIX C

Multiple Scattering Considerations

As described in Sec. IV, the cross sections for the eight elements, Be through U, were fitted with the angular distribution for single scattering, that is, we set

$$N(\theta)=N_0e^{-l(\sigma_T-F_1\sigma_d)}$$
$$=N_0e^{-l\sigma_T}\left\{1+\sum_{n=1}^{\infty}\frac{1}{n!}(l\sigma_d)^nF_1{}^n\right\},\qquad\text{(C-1)}$$

where $N(\theta)=$number of particles emerging from sample within a cone of half-angle θ, $N_0=$number of incident particles, $l=$number of nuclei per unit area, and $F_1(\theta)\equiv F(\theta)=$fraction of single diffraction scattered particles contained in a cone of half-angle θ, as defined in Eq. (8). More accurately one should write

$$N(\theta)=N_0e^{-l\sigma_T}\left\{1+\sum_{n=1}^{\infty}\frac{1}{n!}(l\sigma_d)^nF_n(\theta)\right\},\qquad\text{(C-2)}$$

where $F_n(\theta)=$fraction of n-fold scattered particles contained in a cone of half-angle θ. Using a Gaussian approximation to $F_1(\theta)$, it follows that $F_n(\theta)$ is equal to $F_1(\theta/\sqrt{n})$ in the small angle approximation. Combining Eqs. (C-1) and (C-2), the cross section $\sigma(\theta)$ measured at an angle θ can be expressed as

$$\sigma(\theta)=\sigma_a+(1-F_1)\sigma_d$$
$$-\sigma_de^{-l\sigma_dF_1}\sum_{n=2}^{\infty}\frac{1}{n!}(l\sigma_d)^{n-1}(F_n-F_1{}^n).\qquad\text{(C-3)}$$

The first two terms on the right-hand side form the single scattering approximation to $\sigma(\theta)$, used to fit the data. The third term is the correction due to multiple-diffraction scattering effects. The correction term vanishes both in good- and bad-geometry limits, and, for very thin scatterers it vanishes at all angles. Using the Gaussian, small-angle approximation to $F_n(\theta)$ the corrections to the cross sections are about $\frac{1}{2}$ percent for the scatterer thicknesses and geometries of this experiment.